Journal of Glaciology



Article

Cite this article: Klahold J, Racz GC, Ruols B and Irving J (2026) Imaging englacial and subglacial drainage networks with UAV-based 3D GPR. *Journal of Glaciology* **72**, e42, 1–15. https://doi.org/10.1017/jog.2026.10145

Received: 10 July 2025
Revised: 6 December 2025
Accepted: 28 December 2025

Keywords:
Glacier geophysics; glacier hydrology; ground-penetrating radar

Corresponding author: Johanna Klahold; Email: johanna.klahold@unil.ch

© The Author(s), 2026. Published by Cambridge University Press on behalf of International Glaciological Society. This is an Open Access article, distributed under the terms of the Creative Commons Attribution licence (http://creativecommons.org/licenses/by/4.0), which permits unrestricted re-use, distribution and reproduction, provided the original article is properly cited.

Imaging englacial and subglacial drainage networks with UAV-based 3D GPR

Johanna Klahold, Gabriela Clara Racz, Bastien Ruols and James Irving

Institute of Earth Sciences, University of Lausanne, Lausanne, Switzerland

Abstract

Meltwater drainage through glaciers strongly influences ice dynamics and related hazards, yet detailed observations of active englacial and subglacial networks remain scarce due to challenges in direct observation. We present a novel high-density, UAV-based 3D ground-penetrating radar (GPR) survey of Switzerland's Otemma Glacier, integrated with dye tracing experiments, photogrammetry and hydraulic potential modeling, to map internal water pathways with unprecedented spatial resolution and coverage. Advanced 3D imaging techniques, adapted from seismic diffraction processing, enhance the detection of small-scale conduits within the ice. We identify two primary subglacial channels having distinct hydraulic efficiencies and transport behaviors. Englacial drainage is found to be structurally complex, comprising lateral conduits, branching networks and localized pooling zones. These observations provide critical constraints on the geometry and dynamics of glacier drainage, supporting and extending existing models, and are essential for forecasting glacier behavior under future warming. UAV-based 3D GPR, in combination with novel processing strategies, emerges as an innovative approach for large-scale, repeatable surveys of glacier hydrology.

Introduction

The flow of water through glaciers plays a key role in ice dynamics, influencing processes such as basal sliding, internal deformation and subglacial sediment deformation (Hart and others, 2015). Meltwater storage and movement within the ice also drive transient glacier accelerations, surging behavior and outburst floods (Fountain and others, 2005; Harper and others, 2010). The latter, among other glacier hazards, are expected to become more frequent under a warming climate (Clague and O'Connor, 2021). To better comprehend the associated risks and the overall response of the interplay between glacier dynamics and hydrology to atmospheric warming, it is vital to understand how water is transported through the ice.

Water is largely supplied to the glacial hydrological system through the surface melting of ice and snow. Supraglacial streams form in the ablation zone and enter the glacier through moulins, near-vertical passageways into the englacial environment that typically initiate where streams intersect crevasses (Holmlund, 1988). The formation and evolution of englacial drainage systems have been attributed to a variety of mechanisms, including the propagation of fractures driven by hydraulic pressure (Boon and Sharp, 2003; Alley and others, 2005; van der Veen, 2007), cut-and-closure processes within incised channels (Fountain and Walder, 1998; Gulley and others, 2009a) and the exploitation of existing weaknesses such as debris-laden crevasse traces (Stenborg, 1969, 1973; Fountain and others, 2005; Gulley and Benn, 2007). As suggested by Gulley and others (2009b), individual englacial drainage pathways are likely to arise through a combination of these processes.

Once water reaches the glacier bed, it is routed toward the glacier terminus via the subglacial drainage system, which can range from inefficient, distributed networks to efficient, channelized systems (Fountain and Walder, 1998; Schoof, 2010; Flowers, 2015). Distributed drainage consists of widespread, tortuous pathways such as linked cavities or thin water films that maintain high basal water pressures and promote sliding, whereas channelized drainage transports water through discrete conduits that reduce basal water pressure and sliding velocities. As the melt season progresses and the water supply increases, the subglacial drainage system often transitions from a distributed to a channelized configuration capable of rapidly evacuating water (Hewitt, 2013; Werder and others, 2013; Flowers, 2015). However, transient water pulses from events such as lake drainages or intense rainfall can temporarily overwhelm subglacial drainage networks, causing short-lived increases in basal water pressure and sliding, even within an otherwise efficient channelized system (Iken and Truffer, 1997; Bartholomew and others, 2010).

Current understanding of englacial and subglacial drainage processes has been shaped by a wide array of field observations and modeling efforts (e.g., Werder and others, 2013; Flowers, 2015). However, as the interior and base of glaciers are difficult to access, the observational

https://doi.org/10.1017/jog.2026.10145 Published online by Cambridge University Press

record is limited in spatial extent, resolution and temporal coverage. Valuable point-scale data have come from borehole studies (e.g., Hodge, 1976; Hubbard and others, 1995; Flowers and Clarke, 2002b; Fountain and others, 2005; Rada Giacaman and Schoof, 2023), moulin-based measurements (e.g., Iken, 1972) and from rare excavated tunnels with direct access to the glacier base (e.g., Vivian and Bocquet, 1973; Boulton and others, 1979; Hagen and others, 1993; Lappegard and others, 2006; Lefeuvre and others, 2015). Dye tracing experiments have offered insight into larger-scale hydrological connectivity and transport efficiency (e.g., Nienow and others, 1996b, 1996c, 1998; Hock and others, 1999), and post-deglaciation bed inspections have revealed remnants of former drainage structures (e.g., Walder and Hallet, 1979). Speleological surveys have also been carried out to investigate the inactive drainage system in cases where channels are large and stable enough for physical access (e.g., Benn and others, 2009; Gulley, 2009; Gulley and others, 2009a; Mankoff and others, 2017; Temminghoff and others, 2019). More recently, passive seismic methods have been employed to detect and localize the tremor generated by water flow at the glacier bed, providing information on the migration and enlargement of efficient drainage pathways over the melt season (e.g., Gimbert and others, 2016; Lindner and others, 2020; Nanni and others, 2020).

What is still largely missing from the existing body of literature are high-resolution observations of active englacial and subglacial drainage systems; that is, data that are capable of resolving precise channel morphology, spatial organization and temporal evolution. In particular, key geometric properties of englacial conduits, such as their slope and orientation, remain poorly constrained, as does the connectivity between englacial and subglacial networks. This lack of observational detail limits our ability to validate and refine theoretical models of glacier hydrology, and continues to hinder the development of a more complete understanding of how meltwater is routed through and beneath glaciers.

Ground-penetrating radar (GPR) offers a non-invasive approach to image glacier interiors, leveraging the high dielectric contrasts between water, air and ice to provide high-resolution images of englacial and subglacial structures (Plewes and Hubbard, 2001; Woodward and Burke, 2007; Schroeder and others, 2020). Most commonly, GPR studies on glaciers have involved either two-dimensional (2D) surveys, where data are acquired along individual profile lines, or quasi-three-dimensional (3D) surveys, consisting of parallel 2D profiles spaced well beyond the GPR wavelength (e.g., Arcone and Yankielun, 2000; Moorman and Michel, 2000; Murray and others, 2000; Stuart and others, 2003; Irvine-Fynn and others, 2006; Catania and others, 2008; Bælum and Benn, 2011; Church and others, 2020; Hansen and others, 2020). Although these studies have greatly advanced our understanding of glacier hydrology, such acquisitions struggle to resolve complex structures like drainage networks, in the sense that many details are not captured because of a lack of density of measurements. Furthermore, standard 2D processing methods cannot account for 3D effects in the data, and proper 3D imaging is not possible due to spatial aliasing and the strong directional acquisition bias in quasi-3D measurements (Egli and others, 2021).

3D GPR surveys, consisting of dense parallel profiles spaced on the order of the GPR wavelength, together with a fully 3D processing workflow, are rare in glaciology. However, a small number of studies have shown that they can be highly beneficial for high-resolution imaging of glacier internal structures, revealing details that would otherwise be lost in 2D and quasi-3D acquisitions (Harper and others, 2010; Church and others, 2021; Egli and others, 2021). Church and others (2021) and Egli and others (2021) represent two of the few existing studies that employ 3D GPR to image englacial and subglacial drainage structures. Although the results of this work are highly encouraging, the focus in each study was on a single broad channel, many meters wide, with limited investigation of the larger-scale drainage network and connectivity between features. In addition, conventional foot-based acquisition, as used in these studies, is labor-intensive and inherently limited by crevasses and other hazards, restricting the spatial extent and repeatability of surveys.

Recent advances in both GPR instrumentation and uncrewed aerial vehicle (UAV) platforms have enabled the development of UAV-based GPR acquisition systems for snow and glaciological applications (Valence and others, 2022; Ruols and others, 2023; Selbesoğlu and others, 2023; Tjoelker and others, 2024). Flying just a few meters above the ice at several meters per second, these systems can rapidly collect data over hazardous or obstacle-laden terrain, allowing for high-density coverage with precise differential GPS positioning. In the context of 3D surveys, Ruols and others (2023) highlighted the acquisition of 115 line-kilometers of densely spaced parallel GPR profiles on Switzerland's Otemma Glacier in just four days using a dedicated UAV-based GPR system designed for alpine glacier surveys. The same UAV-GPR system was recently used to monitor the temporal evolution of a surface collapse feature on the Rhône Glacier (Ruols and others, 2025).

In this study, we rigorously process and interpret the high-resolution, high-density 3D GPR dataset from the Otemma Glacier (first presented in Ruols and others (2023)), integrating dye tracing experiments, photogrammetry surveys and hydraulic potential modeling to map englacial and subglacial drainage structures. To enhance the detection of englacial channels, we introduce a new coherence-based diffraction imaging workflow. Subglacial conduits are identified through analysis of the amplitude characteristics of the reflection at the glacier bed. We begin by describing our data acquisition and processing procedure. Next, we present the imaging results, highlighting newly resolved channel networks. Finally, we discuss the hydrological implications of our findings and outline how UAV-based 3D GPR can be further deployed to monitor glacier hydrology and its evolution under climate change.

Study site

This case study was conducted on the Otemma Glacier, one of the largest glaciers in Switzerland with a surface area of 9.2 km^2 and a length of 6.5 km (GLAMOS, 1881-2023). It is a temperate valley glacier located in the southern part of the Valais canton, close to the Swiss-Italian border (Fig. 1). The main glacier has its origin at the southern flank of the Pigne d'Arolla and flows southwest into the Haut Val de Bagnes from about 3790 m to 2500 m above sea level (a.s.l.), while being fed by several tributary glaciers. Most of the glacier volume is located below the equilibrium line altitude, which divides the glacier into a small accumulation zone and a long flat main tongue. The Otemma Glacier is rapidly retreating as a result of climate warming and has been losing mass faster than most glaciers in the Swiss Alps (Fischer and others, 2015). It has been the subject of earlier studies using GPR (Egli and others, 2021) and radio-tagged particle tracking (Jenkin and others, 2023) with the aim of mapping the main subglacial channel. Our survey site is located within the lower ablation area between 2500 m and 2600 m a.s.l., where the maximum ice thickness in 2022 was around

https://doi.org/10.1017/jog.2026.10145 Published online by Cambridge University Press

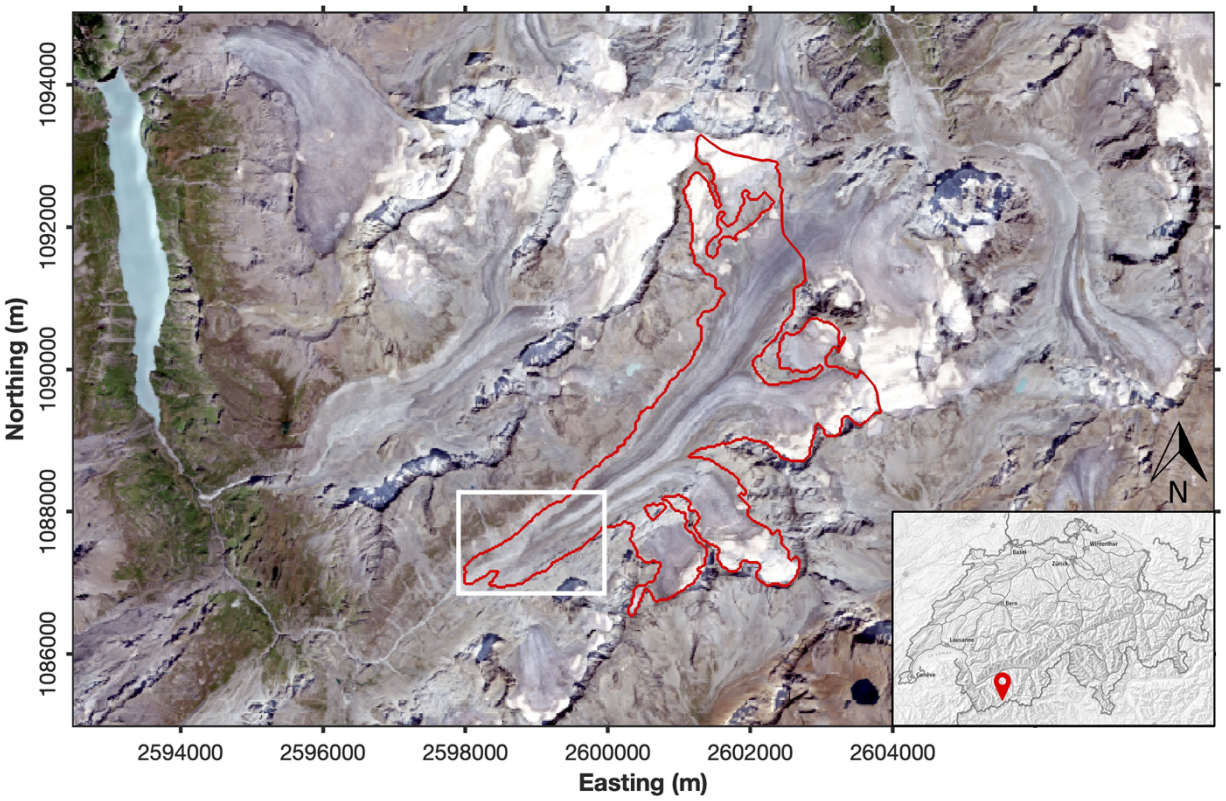


Figure 1. Location of the Otemma Glacier (red outline) in Switzerland (red pin on the insert map). The white rectangle shows the area of our study. The glacier outline on the satellite image corresponds to the most recent GLIMS data (GLIMS Consortium, 2005), and is based on satellite imagery from 2015. The background satellite image was obtained from Copernicus Sentinel data (2022). The insert map was obtained from the Swiss Federal Office of Topography (http://map.geo.admin.ch). All coordinates are given in meters in the local Swiss coordinate system (CH1903+ / LV95).

90 m. Downstream of the survey area, one main subglacial channel emerges at the glacier snout and supplies meltwater to a large turbulent stream known as the Dranse de Bagnes.

Data acquisition and processing

In the summer of 2022, we acquired 3D GPR, photogrammetry and dye tracing data in the lower ablation area of the Otemma Glacier to study its hydrological system. Each of these measurements and its associated data processing is described in detail below. Information is also provided on hydraulic potential modeling, which was carried out based on larger-scale bed topography measurements derived from helicopter-borne GPR surveys (Grab and others, 2021).

3D GPR

GPR acquisition

To investigate the englacial and subglacial drainage network, zero-offset, high-density, 3D GPR data covering an area of approximately 115000 m^2 were acquired near the glacier terminus. The extent of the GPR survey area is shown in Fig. 2. The GPR data were collected over four days (August 2–4 and 6, 2022) using a recently developed UAV-based acquisition system designed for safe and efficient surveying of alpine glaciers (Ruols and others, 2023). The survey grid comprises 488 profile lines spaced at 1 m intervals. This dense line spacing reduces the across-line spatial aliasing of reflected and diffracted arrivals at the antenna's 80 MHz center frequency, which corresponds to a dominant wavelength in ice of approximately 2.1 m. The individual GPR profiles are oriented northwest-southeast, perpendicular to the ice flow direction and vary in length between 115 m and 350 m. In total, more than 115 km of GPR data were acquired.

During data acquisition, the UAV-based GPR system was flown at a height of approximately 5 m above the glacier surface and at a speed of 4 ms^{-1} using the True Terrain Following navigation system from SPH Engineering (Latvia), which uses real-time radar-altimeter measurements to adjust the flight path so that it closely follows the underlying topography (Ruols and others, 2023). With a trace acquisition rate of approximately 14 Hz, stacking each measurement over 5000 times, this configuration yielded more than three GPR traces per meter (Ruols and others, 2023). Data were recorded with a temporal sampling interval of 3.125 ns over a total recording time of 2800 ns, corresponding to a theoretical depth of penetration of approximately 220 m in glacier ice. Ice thickness in the survey area ranged from approximately 20 m to 90 m, and allowed for consistent identification of the glacier bed. The GPR profiles were flown with the single, transmit-receive, resistively loaded dipole antenna oriented perpendicular to the flight direction, which has been shown in previous studies to provide stronger and more coherent bed reflections (Langhammer and others, 2017). The UAV, a DJI M300 RTK drone manufactured by Shenzhen DJI Sciences and Technologies (China), is equipped with a real-time kinematic (RTK) global navigation satellite system (GNSS), providing positioning with a horizontal accuracy of approximately 1 cm and a vertical accuracy of around 2 cm.

https://doi.org/10.1017/jog.2026.10145 Published online by Cambridge University Press

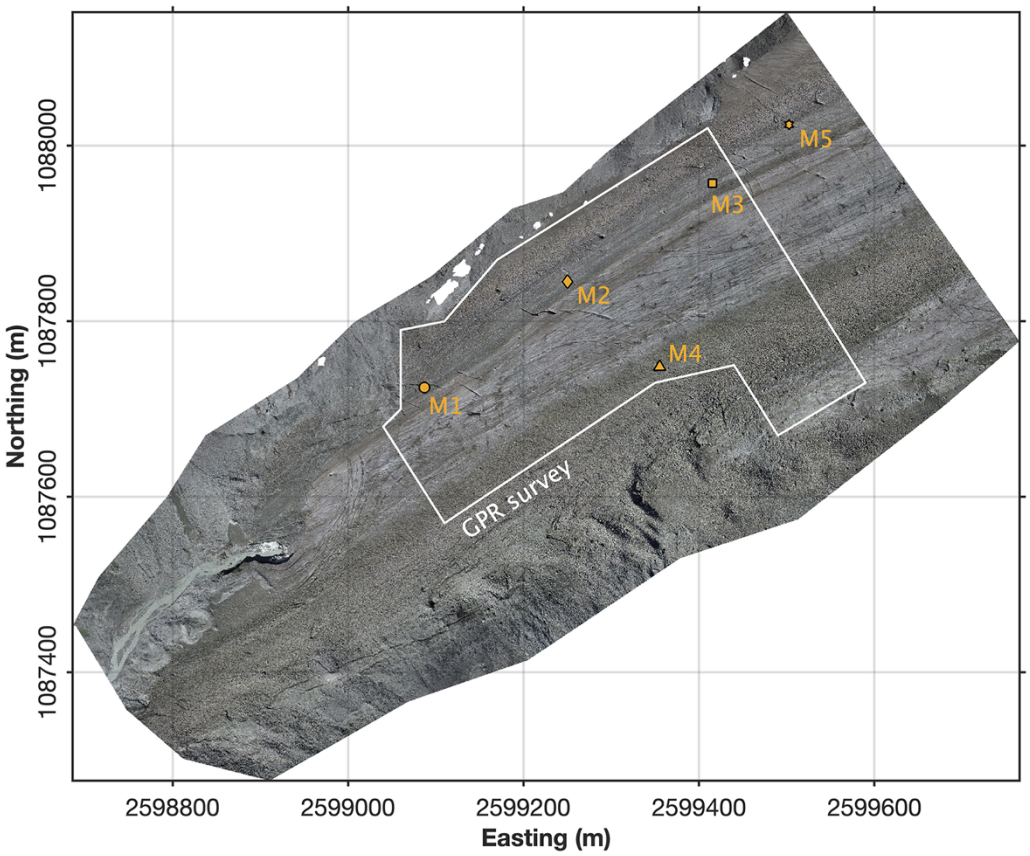


Figure 2. Study site close to the glacier terminus. The white polygon indicates the area covered by the GPR survey. The orange symbols mark the locations of moulins that were used for dye tracing experiments. The background orthomosaic was obtained from photogrammetry surveys conducted in September 2022.

GPR processing

The raw GPR measurements, which are recorded in time, were processed to produce two separate depth-migrated 3D data volumes: a reflection volume to map the topography of the glacier bed and the locations of subglacial channels, and a diffraction volume to identify englacial features. The processing workflow is accordingly divided into two parallel streams to produce these volumes. Both processing streams share an initial set of basic preprocessing steps (Fig. 3).

Preprocessing.

GPR acquisition with our UAV-based system requires additional preprocessing steps beyond those used in conventional surface-based surveys (Ruols and others, 2023). In the field, GPR traces and drone navigational data are recorded separately, each tagged with GPS time. The first step is to synchronize these datasets based on the shared timestamps for each flight, such that each recorded GPR trace is associated with full navigational information. Next, the GPR data are segmented into individual profile lines, and binning is performed using the trace positioning data to distribute the GPR measurements evenly along each line. In this regard, we adopted an along-line bin spacing of 0.4 m which, given our UAV speed and the GPR sampling rate, ensured a sufficiently high trace density to populate every bin. Stacking the binned profiles side by side produces an initial 3D GPR volume, which requires further positional corrections to address artifacts introduced during UAV acquisition. Discontinuities in the data between profile lines, related to small changes in flight altitude, are corrected using Fourier static adjustments in order to simulate a smooth acquisition surface. Lateral positioning corrections are applied to address systematic shifts between odd- and even-numbered profiles related to small internal timing delays specific to our GPR controller. The latter is accomplished using a constrained cross-correlation algorithm that maximizes continuity between adjacent profiles (Ruols and others, 2023). For full details on these preprocessing steps, see Ruols and others (2023, 2025).

After the drone-specific processing described above, the following standard GPR processing is applied to each profile: (i) mean trace removal using a 100-trace sliding window, (ii) de-wow using a 35-point residual median filter, (iii) 4 times temporal densification via Fourier transform interpolation, (iv) time-zero correction, (v) application of a smooth mute to the initial part of each trace and (vi) a second mean trace removal using a 15-trace sliding window applied to the upper portion of the profiles to further suppress residual ringing artifacts. Figure 4a shows an example GPR survey line after application of these steps, where we observe a clear reflection from the glacier bed as well as numerous diffraction hyperbolas arising from englacial scatterers.

Reflection analysis.

To image the subglacial drainage system, we first follow Egli and others (2021) and Ruols and others (2025) and apply 3D topographic time migration to the GPR data using the algorithm developed by Allroggen and others (2015), which is based on the general Kirchhoff scheme presented in Schneider (1978). To account for the distance between the GPR antenna and the glacier

https://doi.org/10.1017/jog.2026.10145 Published online by Cambridge University Press

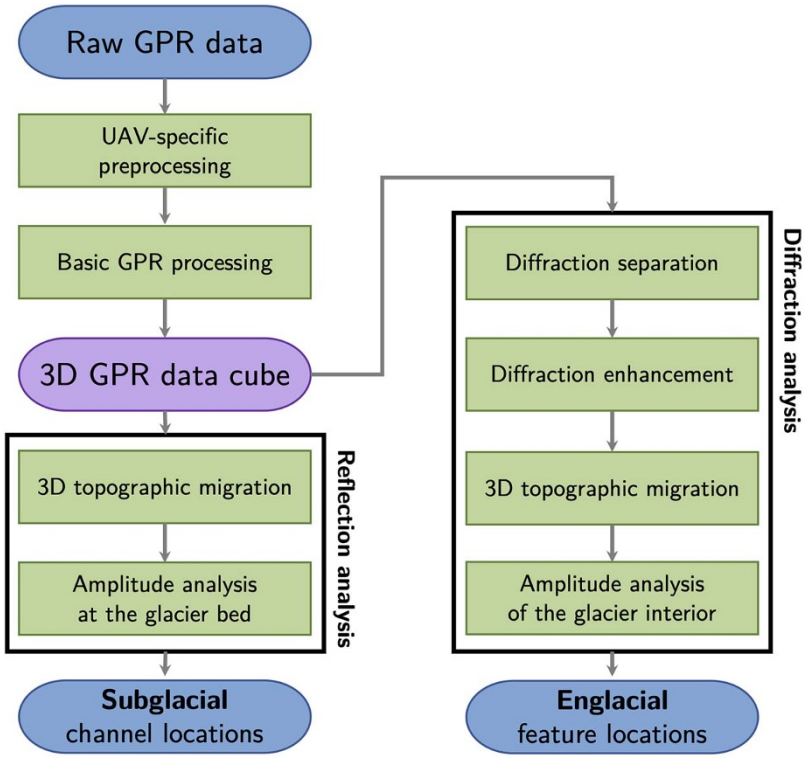


Figure 3. Overview of the GPR data processing workflow. Left: Reflection analysis stream used to map subglacial channels. Right: Diffraction analysis stream used to identify englacial features. Both streams share a common set of initial preprocessing steps.

surface, we consider a two-layer migration velocity model. The upper layer represents air, with a velocity of 0.3 m ns^{-1}, whose thickness is determined from the UAV's altimeter data following Ruols and others (2025). The lower layer corresponds to glacier ice, for which we assume a constant velocity of 0.16 m ns^{-1}, as is commonly done in glaciological GPR studies (e.g., Bradford and others, 2009; Langhammer and others, 2017; Church and others, 2020). Velocity testing showed that this value provides the most coherent collapse of diffraction hyperbolas during migration. Additional testing indicated that a migration aperture of 40 m effectively collapses diffraction hyperbolas in the dataset. Following migration, the same two-layer velocity model is used to convert the data from time to depth, and the position of each trace is shifted vertically to account for the topography of the acquisition surface. Figure 4c shows the example profile from Fig. 4a after migration, time-to-depth conversion and topographic correction.

To map subglacial channels, we use the migrated 3D GPR volume to delineate and analyze the glacier bed reflection (Church and others, 2021; Egli and others, 2021; Ruols and others, 2025). Channels filled with water or air produce a stronger contrast in dielectric permittivity with the glacier ice than the surrounding bedrock, which results in a greater radar reflection coefficient in the channel locations. To this end, we manually pick the ice–bed interface on the individual migrated GPR profiles, and we use local linear regression to produce a smooth bedrock surface model (Fig. 4c). To quantify reflection strength at the bed, we calculate the instantaneous amplitude of each trace using the Hilbert transform (Taner and others, 1979; Chopra and Marfurt, 2007), and identify its maximum over a vertical 2 m window centered on the identified bedrock location (Egli and others, 2021; Ruols and others, 2025). The resulting maximum instantaneous amplitude values typically exhibit a small but systematic decrease with increasing ice thickness, reflecting the greater loss of radar energy with increasing propagation distance. To correct for this effect, we apply robust linear regression to estimate and remove the thickness-related trend. We acknowledge that some redistribution of energy by englacial reflections is possible and may locally influence the amount of energy reaching the bed; however, in practice, we have not found this to limit the identification of subglacial channels in our data. We further acknowledge that the data were collected over several days, but we do not observe diurnal variations in the nature of the data that would affect the imaging or interpretation of the larger-scale drainage network. The final product is a 2D map of maximum reflection strength along the glacier bed.

Diffraction analysis.

GPR data acquired over temperate glaciers are typically rich in diffraction events caused by englacial heterogeneities that act as either point or line scatterers of the radar energy (Murray and others, 2000; Schaap and others, 2020; Ogier and others, 2023). Imaging these events in 3D and analyzing their spatial distribution can serve as a potentially powerful tool to characterize the glacier's drainage system, as englacial channels and voids will act as strong scatterers due to the marked contrast in dielectric permittivity with their surroundings. To identify englacial features, we thus focus on diffracted energy within the preprocessed 3D GPR data cube. To distinguish diffraction signals from reflections and noise in a fully data-driven manner, we adopt the coherent stacking scheme of Schwarz and Gajewski (2017) and Schwarz (2019). The corresponding workflow comprises two main steps: diffraction separation and diffraction enhancement. For computational efficiency, both steps are applied to individual 2D GPR profiles. The processed profiles are then reassembled into a 3D data cube, which is subsequently migrated in 3D to accurately image diffracting features.

In the first step, we separate diffracted energy from reflected signals by performing a coherent summation within a defined

https://doi.org/10.1017/jog.2026.10145 Published online by Cambridge University Press

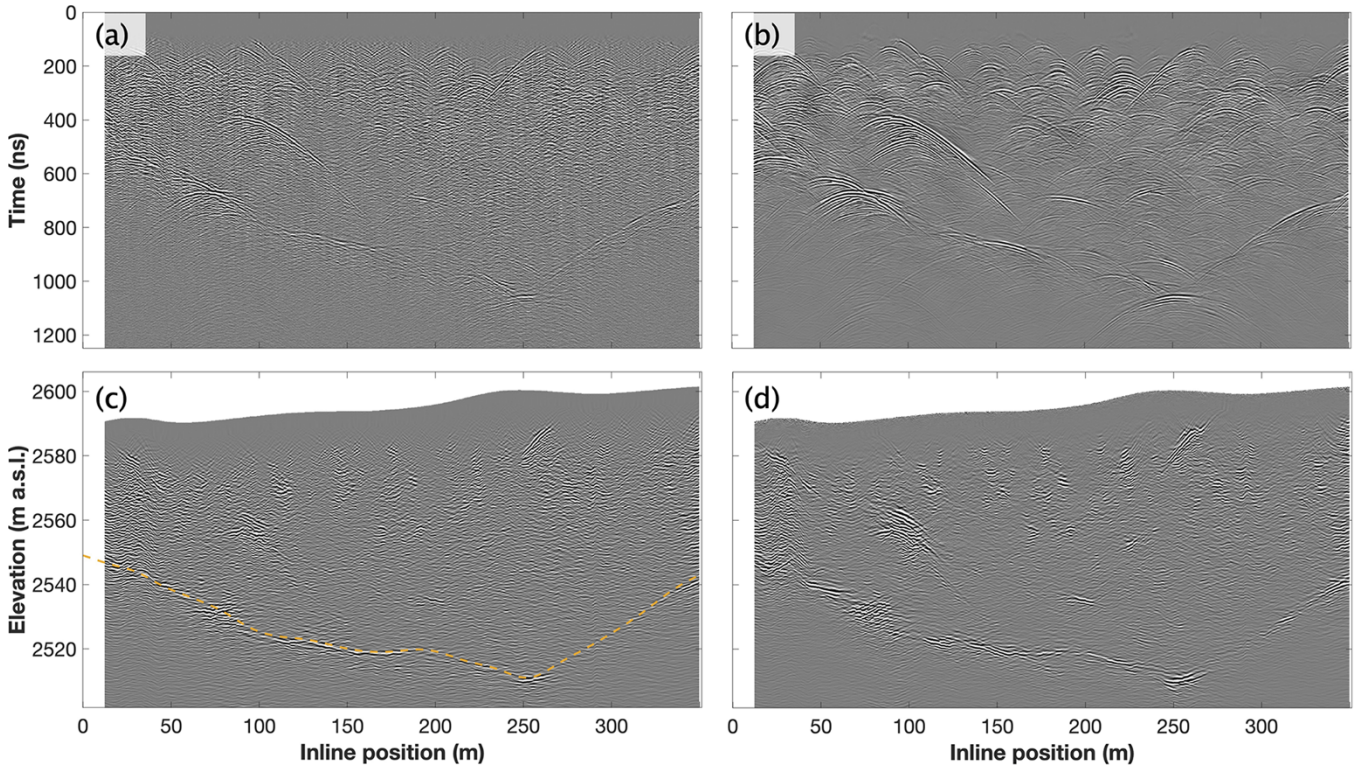


Figure 4. Demonstration of the GPR processing for one example inline profile located at a crossline position of 459 m: (a) after preprocessing; (b) result from (a) after diffraction separation and enhancement; (c) result from (a) after 3D topographic migration, time-to-depth conversion and topographic correction, with the orange line indicating the smooth bedrock surface model developed from the picked glacier bed reflection; (d) result from (b) after 3D topographic migration, time-to-depth conversion and topographic correction.

aperture around each data sample. Local slopes and curvatures of emerging wavefronts are estimated directly from the data using a coherence maximization procedure. Since reflections generally exhibit lower slope and curvature values than diffractions, we can distinguish between the two using threshold-based filtering. We apply directional stacking, which inherently favors the dominant reflected arrivals, and combine this with a slope-based filter to estimate the reflected component. The estimated reflected wavefield is then subtracted from the original data, resulting in a GPR profile that contains primarily diffracted energy, along with residual noise (Schwarz and Gajewski, 2017; Schwarz, 2019). In the second step, to further enhance the diffraction signal, we re-estimate slope and curvature attributes from the resulting diffracted wavefield and use them to guide a second coherent stacking step, this time optimized to emphasize locally coherent diffraction events. Figure 4b shows the preprocessed example profile from Fig. 4a after diffraction separation and enhancement, where we see that the diffractions can be much more easily identified and that clutter-type noise in the section has been greatly reduced.

The separated and enhanced diffraction data are subsequently imaged through 3D topographic migration using the same algorithm as in the reflection analysis (Allroggen and others, 2015). For this step, we employ a slightly larger migration aperture of 50 m to better capture the wider spread of diffracted energy in the enhanced data, while all other migration parameters remain unchanged. Figure 4d presents the diffraction enhanced survey profile from Fig. 4b after migration, time-to-depth conversion and topographic correction, where we observe that the migration algorithm effectively collapses diffraction hyperbolas around their primary scattering points.

The separated, enhanced and migrated GPR diffraction volume is analyzed to identify drainage pathways within the glacier interior, which typically correspond to regions of high amplitude that exhibit strong spatial continuity across multiple survey profiles. To this end, similar to the subglacial analysis, we first calculate the instantaneous amplitude of each trace in the volume using the Hilbert transform, which serves as a proxy for scattering strength. Next, we apply a thresholding step by selecting the 99th percentile of normalized amplitude values, in order to isolate only the highest-amplitude features likely to represent strong scatterers such as channels. We then use a 3D elliptical structuring element on the resulting binary volume to perform morphological closing, connecting nearby high-amplitude regions. Connected components are extracted from the closed volume using 26-connectivity. Finally, for each component, we compute geometric properties such as volume and principal axis length, and retain only elongated structures having a principal axis length greater than 30 voxels and a volume exceeding 2500 voxels, yielding a binary mask of candidate englacial channels with unique feature IDs.

Photogrammetry

High-resolution UAV-based photogrammetry surveys were conducted on September 12, 2022, to generate an orthomosaic and a digital elevation model (DEM), providing surface information to support the interpretation of the UAV-based GPR data. A DJI Phantom 4 Pro UAV was flown at altitudes between 65 and 80 meters above the take-off point, capturing nadir and oblique imagery. Approximately 2,000 images were acquired. A differential

https://doi.org/10.1017/jog.2026.10145 Published online by Cambridge University Press

GPS (Topcon GR-5) was used to survey the precise positions of 15 ground control points (GCPs), along with 22 additional check points (CPs) used for model validation.

The data were processed using the Agisoft Metashape Professional Edition 2.1.2 software, largely following the guidelines provided in the user manual. The photogrammetric processing workflow included image quality assessment, photo alignment, point cloud generation and model optimization based on GCPs. Photo alignment was performed using a key point limit of 120,000 and a tie point limit of 12,000, with adaptive camera model fitting enabled. Dense point clouds were generated using depth maps at high quality with moderate depth filtering. The dataset was georeferenced using the Swiss coordinate system (CH1903+ / LV95). The final DEM has a spatial resolution of 4.96 cm/pixel, whereas the resolution of the orthomosaic is 2.48 cm/pixel.

Dye tracing

To investigate englacial and subglacial drainage connections in our study region, we conducted six dye tracing experiments using two fluorescent tracers: rhodamine WT and fluorescein. The experiments were conducted between August 2 and 6, with individual injections performed at different times of day. The tracers were injected simultaneously into selected pairs of moulins in the survey area (M1–M5; Fig. 2), which allows us to compare the connectivity of the moulins to the subglacial system and the efficiency of the drainage pathways. The moulins were selected because of their high observed meltwater input. Injection times were synchronized to the second to ensure similar flow and discharge conditions, which vary substantially throughout the day, even on the time scale of minutes. Repeat experiments were conducted for the moulin pair M1–M2 to assess the consistency of the results across multiple days and times of day. For all experiments, the dye concentrations were measured in the main outlet stream close to the glacier terminus with a fluorometer (Albillia GGUN-FL30) recording at 6 s intervals after dye injection. Breakthrough curves were generated by applying a 60 s running average filter to the measured dye concentrations, subtracting any instrument bias to read a background value of zero, and scaling by the maximum dye concentration value over all breakthrough curves of the same dye type. The curves were analyzed following Nienow and others (1996a) in order to estimate the arrival time (t_a), the peak arrival time (t_m), and the water throughflow velocity (u).

Hydraulic potential modeling

As an independent method to assess the plausibility of the subglacial drainage system inferred from the 3D GPR data, we estimated the likely subglacial water routing following the approach of Shreve (1972), which assumes that subglacial flow paths are governed by the spatial distribution of the hydraulic potential at the bed, ϕ, given by

$$\phi = \rho_w g z_b + p_w, \quad \text{with} \quad p_w = \alpha \rho_i g (z_s - z_b), \tag{1}$$

where p_w is the subglacial water pressure at the ice-bed interface, assumed to be a fraction α of the ice overburden pressure, ρ_w is the density of water (1000 kg m^{-3}), ρ_i is the density of ice (917 kg m^{-3}), g is gravitational acceleration (9.81 m s^{-2}), z_s is the ice surface elevation and z_b is the bedrock elevation. Here, we assumed $\alpha = 1$, which corresponds to the common assumption that water pressure is equal to ice overburden pressure (i.e., a steady-state or 'full' subglacial water system). We used surface and bedrock topography data from Grab and others (2021) at 10 m horizontal resolution for this analysis, rather than our own derived surface and bed topography data over the GPR survey region, because coverage across the entire glacier domain was required to calculate flow pathways beyond the limited survey area.

From the calculated hydraulic potential field, we derived local hydraulic gradients and flow directions using the `TopoToolbox` package in MATLAB (Schwanghart and Kuhn, 2010; Schwanghart and Scherler, 2014). Treating the hydraulic potential as an analog to topographic elevation, the `D8` (Deterministic Eight-Neighbor) flow routing algorithm (O'Callaghan and Mark, 1984) was employed, which routes the flow from each grid cell to its single steepest downslope neighbor. Once the flow directions were determined, we applied the `flowaccumulation` function to estimate the upstream contributing area for each grid cell, which yields insight into likely subglacial drainage networks and relative discharge magnitudes.

Results

Subglacial drainage system

Figure 5 presents the results of our GPR reflection analysis. In Fig. 5a, we show the glacier bed elevation determined from manual picking of the ice-bed interface along each profile in the migrated 3D reflection volume. The glacier surface elevation is shown in Fig. 5b. Taking the difference between these quantities yields the ice thickness in the survey region (Fig. 5c), which is seen to vary between 20 m and 90 m. In Figure 5d, we show the 2D map of normalized reflection strength along the glacier bed. Here, we can identify two distinct zones exhibiting higher amplitude reflections than their surroundings, interpreted as potential subglacial channels, that run from northeast to southwest across the entire GPR survey region, broadly aligned with the direction of glacier flow. The northern zone, hereafter referred to as channel A, initially appears weakly up-glacier in the vicinity of moulin M3. As it continues down-glacier, its signature becomes stronger and, after meandering slightly, it follows a trajectory roughly parallel to the northern glacier flank. Near the western edge of our survey region, channel A exhibits a pronounced southward meander around the location of moulin M1. The second distinct, high-reflectivity zone to the south, hereafter referred to as channel B, is clearly visible in the eastern-most part of the survey region. It initially follows the deepest section of the basal topography, undergoes a sharp bend, and then continues along a straight trajectory that passes below moulin M4. Further downstream, channel B appears to widen and eventually meanders northward to coalesce with channel A near the western edge of the survey area, where an ice-marginal channel is visible further along the inferred trajectory (Fig. 2). Notably, our dye tracing moulins also appear to be positioned broadly above these channels, reinforcing the link between the GPR-identified basal features and glacier drainage. Additionally, along the north and south boundaries of the survey region, we observe further high-amplitude zones. However, the available data do not allow us to determine whether these features are representative of actual basal conditions or artifacts introduced during migration.

Figure 6 shows the breakthrough curves obtained for the six dye tracing experiments that were conducted for various pairs of moulins. Table 1 presents metrics obtained from a quantitative analysis of these curves. We observe a clear dye breakthrough for all injected moulins (M1–M5), indicating that each is hydraulically

https://doi.org/10.1017/jog.2026.10145 Published online by Cambridge University Press

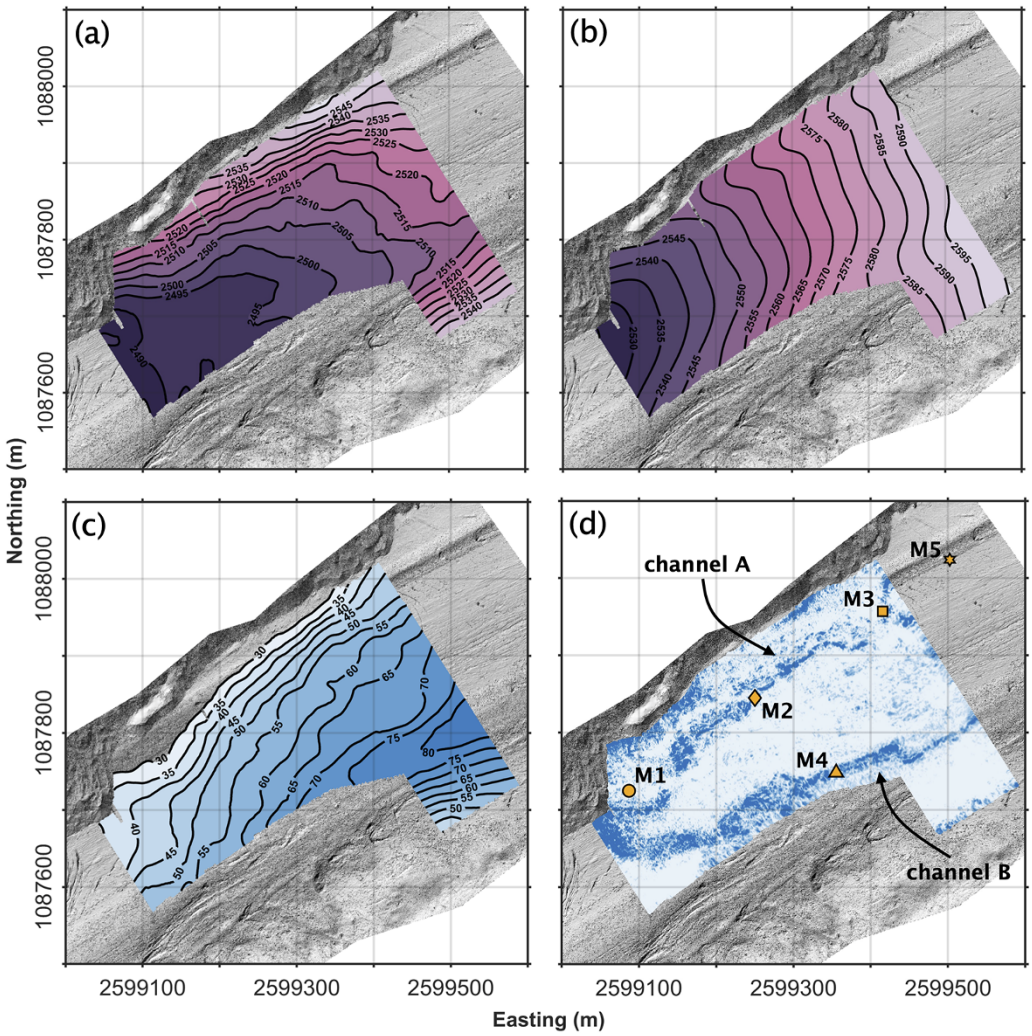


Figure 5. GPR reflection analysis results: (a) glacier bed elevation (m a.s.l.); (b) glacier surface elevation (m a.s.l.); (c) calculated ice thickness (m); (d) normalized reflection strength along the glacier bed (blue = stronger). All images are superposed on a hillshade of the DEM from September 2022.

connected to the main subglacial drainage system. This is also reflected in the rapid throughflow velocities ($u > 0.2\,\mathrm{m\,s^{-1}}$, Burkimsher (1983)) for all injection points, namely, for moulins M1, M2, M3 and M5, which are likely connected to channel A, and for moulin M4, which is presumably linked to channel B. Overall, dye arrival times increase progressively with distance up-glacier, reflecting longer travel paths for upstream moulins. One notable exception is moulin M4, which exhibits a markedly greater arrival time and a lower throughflow velocity than moulin M2, despite being located at a comparable distance from the glacier snout. This suggests that either moulin M4 has a less direct connection to the subglacial channel, or that channel B is less hydraulically efficient than channel A. Channel B may indeed exhibit a greater potential for dispersion than channel A, as suggested by the broader breakthrough curve of moulin M4 compared with moulin M2.

Another experiment that merits closer attention is the comparison between the breakthrough curves of moulins M3 and M5. A sharp, well-defined breakthrough curve is observed for moulin M5, whereas moulin M3 exhibits a broader curve with a longer tail (Fig. 6). This contrast suggests that M5 may drain directly into the main subglacial conduit, whereas M3 could be connected via a smaller tributary channel. However, moulin M5 lies outside the GPR survey area, making it difficult to verify its connection to the main drainage system. This inference is further limited by the fact that only a single dye tracing experiment was conducted for the M3–M5 pair, and the resulting travel times may have been affected by local injection conditions. Additionally, while dye tracing provides valuable insights into subglacial drainage efficiency, it is important to recognize that dye must first traverse the englacial system before reaching the bed. This englacial component is often neglected in analyses and may introduce uncertainty into interpretations based solely on travel time and flow velocities.

Finally, repeat tracer injections for moulin pair M1–M2 reveal consistent breakthrough behavior across different times of day and on separate days (evening on August 2, midday and afternoon on August 4). While slight variations in curve shape and timing are observed, moulin M1 consistently exhibits an earlier arrival than moulin M2, and both moulins produce two sharp breakthrough peaks. This suggests a temporally stable drainage configuration during the observation period, demonstrating the robustness of dye tracing across the days of data collection and justifying its use for inferring overall drainage characteristics.

https://doi.org/10.1017/jog.2026.10145 Published online by Cambridge University Press

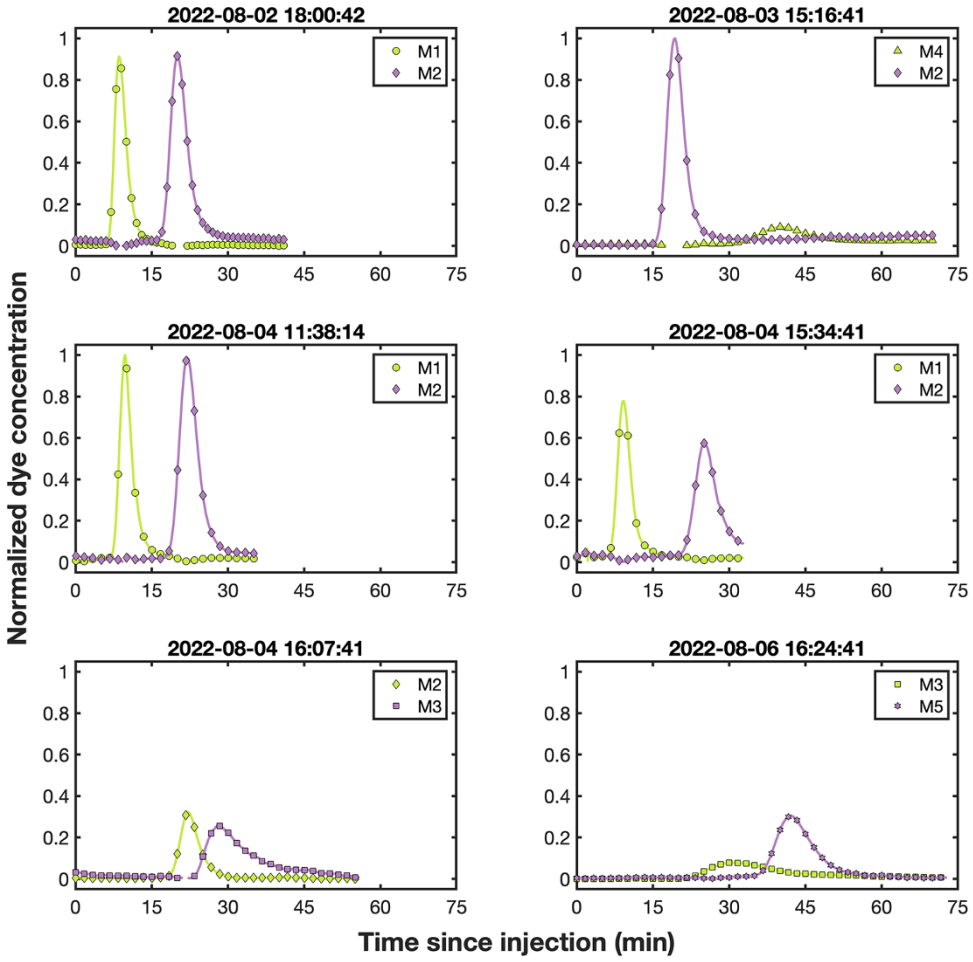


Figure 6. Dye concentration over time for six dye tracing experiments involving pairs of moulins. Colors and symbols are representative of the injected dye (lilac: rhodamine WT, green: fluorescein) and moulin, respectively.

Table 1. Dye tracing metrics calculated from the breakthrough curves presented in Figure 6 following Nienow and others (1996a). Shown are the straight-line distance between the moulin and the glacier outlet (L), the tracer arrival time (t_a), the peak arrival time (t_m) and the water throughflow velocity (u). For moulins with repeat injections, mean values of the metrics were calculated.

Moulin	L (m)	t_a (min)	t_m (min)	u ($m\,s^{-1}$)
M1	354.0	6.6	9.3	0.90
M2	556.6	17.6	21.9	0.53
M3	756.2	21.9	30.9	0.58
M4	598.0	31.5	41.0	0.32
M5	866.0	35.2	42.7	0.41

Figure 7 presents the results of our hydraulic potential modeling, and highlights the most probable locations of subglacial channels based on the underlying bedrock topography and ice thickness data of Grab and others (2021). Two main channels can be identified, which merge downstream; the northern channel appears to accumulate a greater volume of water and may function as the primary drainage pathway. We observe that the modeled subglacial drainage network exhibits strong spatial correspondence with the regions of increased GPR bed reflection amplitude (Fig. 7; inset), suggesting that the drainage patterns inferred from the GPR data are physically plausible and likely represent actual subglacial flow paths. Again, dye tracing moulins M1–M5 lie broadly atop the modeled subglacial channels. However, it is important to note that this analysis reflects a stationary and steady-state assumption, where the hydraulic potential field is considered time-invariant, which is a strong simplification. In reality, subglacial water pressure and routing pathways vary temporally due to meltwater input fluctuations, ice dynamics and evolving drainage system configurations. Therefore, the modeled pathways represent only a static and idealized scenario.

Englacial drainage system

Figure 8 presents the results of our diffraction analysis, which yields a 3D map of connected zones of high scattering amplitude that we interpret as components of the englacial drainage network. From a top-down perspective, many of the englacial features exhibit a linear alignment roughly along the glacier flow direction (Fig. 8a). In the 3D view, we see that the internal architecture is complex, consisting of a number of variable-sized features that likely share further connections that are not imaged (Fig. 8b). Note that many of the identified englacial features and moulin locations do not directly overlie the main subglacial channels identified in our bed reflection analysis. This, along with the observation that the englacial channels span large horizontal distances, suggests that meltwater is not routed vertically from the surface to the bed, but instead travels laterally through the englacial system, often over considerable distances, before entering the main subglacial channels.

https://doi.org/10.1017/jog.2026.10145 Published online by Cambridge University Press

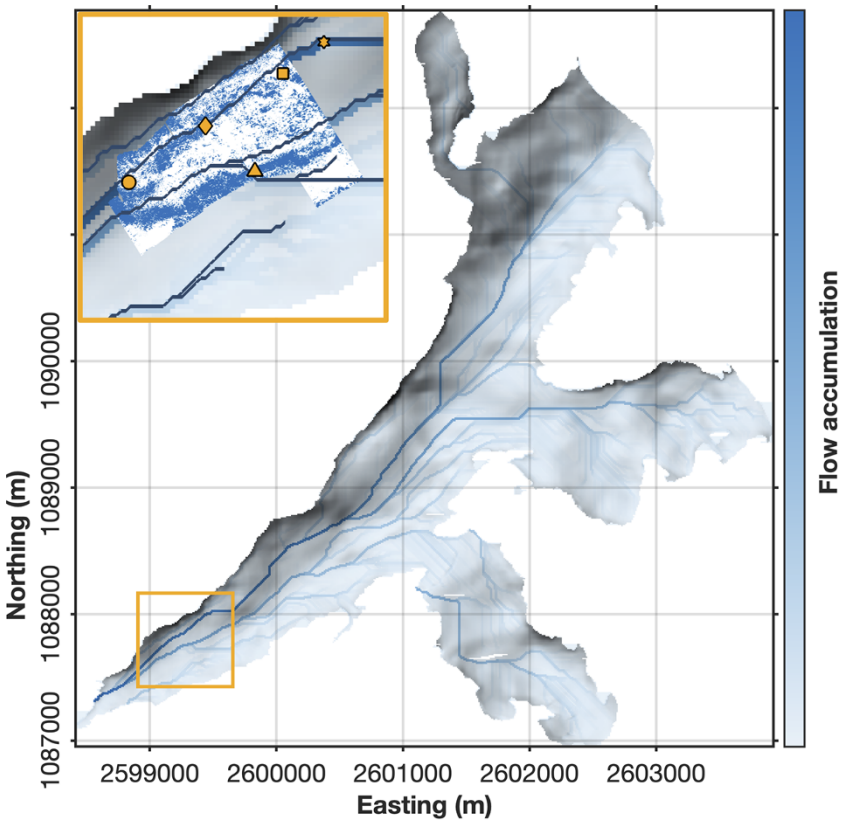


Figure 7. Most probable subglacial channel locations according to the Shreve hydraulic potential model. Shading reflects the amount of flow accumulation, with darker blue representing higher accumulated flow and thus a higher likelihood of subglacial drainage pathways. The inset shows a zoom of the GPR survey area with an overlay of the normalized GPR reflection strength at the glacier bed. Orange symbols indicate the locations of dye tracing moulins, whereas dark blue lines mark the main flow accumulation drainage paths.

To explore further, we highlight two representative features, isolated using their feature IDs, which are presented in Figs. 9 and 10. The first feature (Fig. 9) is a well-defined englacial channel oriented approximately along the glacier flow direction (i.e., parallel to the crossline axis), with a total length of nearly 200 m. Located about 20 m below the ice surface, the channel maintains a consistent, linear geometry but exhibits notable variations in its longitudinal slope that likely influence internal water flow dynamics. In its uppermost section, the channel descends gently with a slope of approximately 3° over a distance of approximately 80 m. The gradient then steepens significantly to around 9° over 70 m, before decreasing slightly to about 8° over 50 m. Moulins observed at the surface above the channel suggest that it may be actively fed by these surface meltwater inputs. In its lower section, at a crossline position of 250 m, the englacial channel appears to become more diffuse, connecting with a set of narrower, parallel side channels (not displayed in the reduced 3D view in Fig. 9a). These smaller conduits run roughly in the same direction and may function as secondary flow paths, suggesting a sectional branching structure within the englacial system. Downstream of this, at a crossline position of around 170 m (Fig. 9c), the main englacial channel exhibits a sudden vertical drop into a localized region of high reflectivity, which we interpret as a potential water pooling area. While we do not directly observe a connection to the subglacial system within the GPR volume, it is likely that this channel ultimately links to the basal drainage network, given its alignment and downward trajectory. This interpretation is supported by the presence of a stronger glacier bed reflection in the crossline radar profiles, especially near the terminus, where high reflectivity is consistent with the position of the subglacial channel identified in previous analyses.

The second feature (Fig. 10) is interpreted as a localized englacial pooling structure about 30 m below the glacier surface, approximately 20 m wide in the cross-glacier direction and 50 m long along the direction of glacier flow. The feature is clearly resolved in both the inline and crossline depth sections in Figs. 10d and 10e, respectively, as shown by a concentrated zone of high reflectivity within the ice. Several moulins are located directly above and around this feature, suggesting active surface meltwater input. It is likely that water is routed downwards beneath at least one of these moulins into the pooling region. Additionally, the feature appears to be fed by a horizontal englacial connection from further up-glacier, as indicated by the smeared-out high-amplitude zone near the uppermost edge of the survey area. The pooling structure is situated just above the location of the main subglacial channel, making a hydraulic connection between the two likely. However, the identification of vertical conduits is inherently constrained by the limitations of our GPR survey geometry, which restricts sensitivity to near-vertical features. Notably, this pooling feature lies adjacent to moulin M3, one of the dye tracing injection points. Yet, the slight offset of moulin M3 suggests that more likely one of the adjacent moulins and not moulin M3 directly feeds the pooling feature. The connection from moulin M3 may be more complex or less efficient, potentially contributing to the higher dispersion observed in the dye tracing results.

Discussion

This study integrates high-density 3D GPR, dye tracing, photogrammetry and hydrological modeling to investigate the englacial and subglacial drainage system of a temperate alpine

https://doi.org/10.1017/jog.2026.10145 Published online by Cambridge University Press

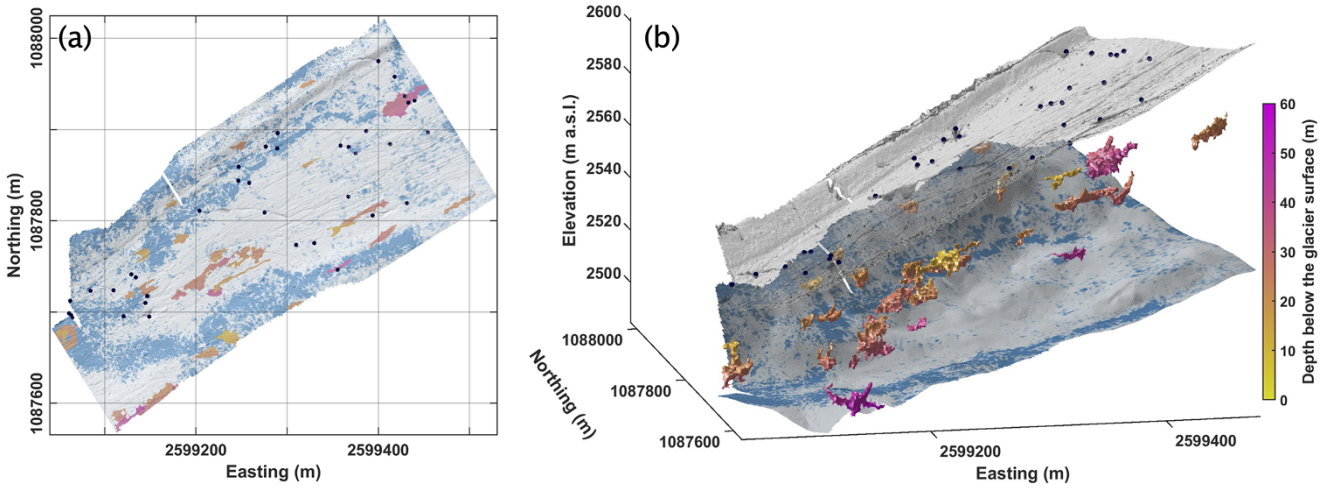


Figure 8. 3D map of spatially connected high-amplitude zones in the GPR diffraction instantaneous amplitude volume. The glacier surface is provided by the DEM from September 2022. The glacier bed is provided by our GPR bed reflection analysis, and is shaded with the map of normalized reflection strength. Black dots at the glacier surface indicate moulin locations identified on the orthomosaic (Fig. 2). (a) Top view; (b) side view.

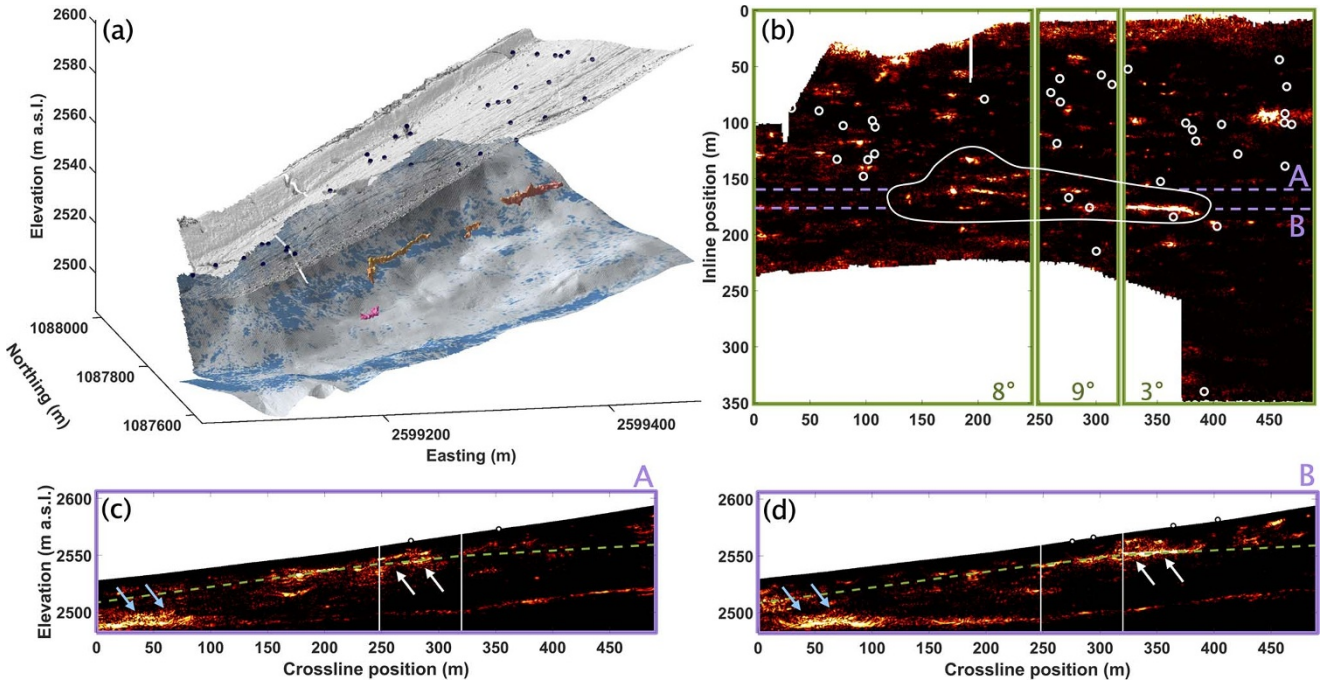


Figure 9. Englacial feature 1: (a) 3D map of the isolated feature; (b) composite plan view of three slices through the diffraction instantaneous amplitude volume at different angles with respect to the horizontal; (c) crossline slice through the volume at an inline position of 161 m; (d) crossline slice through the volume at an inline position of 176 m. Dots denote identified moulin locations. White arrows and outline highlight the englacial channel. Blue arrows indicate the region of stronger bed reflection amplitude.

glacier. With regard to the subglacial network, all methods consistently support the hypothesis of two main subglacial pathways beneath the study area (channels A and B). The positions of these channels identified from the GPR data correspond well with the flow paths estimated from our hydraulic potential analysis. The dye tracing experiments confirm rapid throughflow for most moulins, supporting the existence of efficient subglacial routing, particularly via channel A. Channel B exhibits higher dispersion and lower velocities, suggesting more distributed or complex drainage characteristics, with potential storage zones or side connections that delay tracer transport compared to the more efficient, well-channelized flow in channel A. With regard to the englacial drainage network, our 3D GPR diffraction analysis reveals a structurally complex system within the ice, characterized by defined channels with variable slopes, localized pooling zones and branching networks. These features indicate that meltwater is not routed directly vertically from the surface to the bed, but rather travels considerable distances englacially before reaching the subglacial system. The spatial configuration of the identified englacial drainage pathways suggests that the englacial structures feed into the imaged subglacial pathways, although the exact points of connection remain unresolved in our GPR data. Despite the use of high-density 3D GPR, spatial resolution remains constrained by the radar wavelength and the inherent limitations

https://doi.org/10.1017/jog.2026.10145 Published online by Cambridge University Press

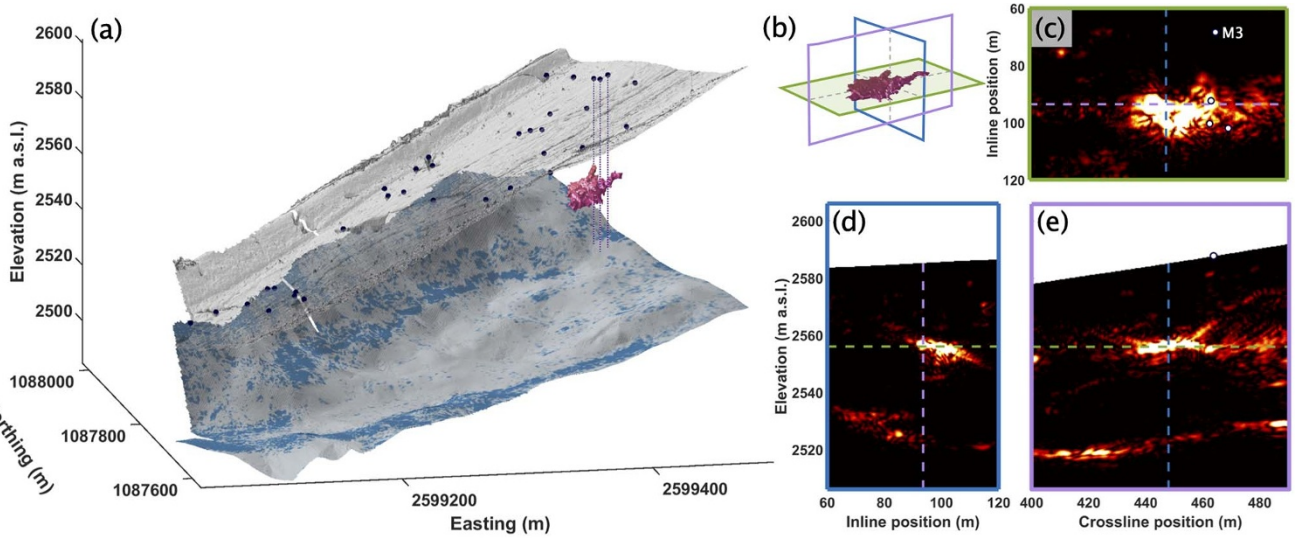


Figure 10. Englacial feature 2: (a) 3D map of the isolated feature; (b) geometry of the presented data slices; (c) horizontal slice through the diffraction instantaneous amplitude volume at an elevation of 2556 m a.s.l.; (d) inline slice through the volume at a crossline position of 448 m; (e) crossline slice through the volume at an inline position of 94 m. Dots denote identified moulin locations.

of migration in complex glacial environments. As a result, features smaller than 1–2 m may not be fully resolved, contributing to uncertainties in mapping fine-scale drainage connectivity.

A key contribution of our study is the high-resolution, 3D imaging of lateral englacial routing and localized pooling structures within an active, hydrologically connected glacier system. While it is now recognized that meltwater does not always travel vertically from surface moulins directly to the bed (e.g., Gulley and others, 2009b; Temminghoff and others, 2019; Schaap and others, 2020), few studies have visualized these pathways in such detail. The prominent englacial channel feature (Fig. 9) exhibits slope variations that may influence flow velocity, possibly accelerating drainage through the steeper sections while encouraging temporary water retention or pooling where gradients shift. In conjunction with the second key feature, the localized pooling structure (Fig. 10), these observations suggest that englacial conduits may function as temporary storage reservoirs or slow-release pathways, potentially modulating the timing and variability of meltwater reaching the bed. This has important implications for interpreting dye tracing data, which typically assume direct surface-to-bed flow and may underestimate englacial transport delays.

The GPR-based methodology presented in this work may also contribute to the refinement of glacier hydrology models in the future by providing empirical constraints on the spatial organization of internal water pathways. By imaging englacial structures that likely govern subglacial water delivery, we provide observational support for theoretical models that incorporate englacial routing and storage (e.g., Bartholomaus and others, 2008; 2011; Hewitt, 2013; Werder and others, 2013), and offer evidence to improve their representation in large-scale simulations. The observed spatial offset between some moulin locations and subglacial channel positions indicates that surface inputs alone are not reliable predictors of basal water entry points. Consequently, our results challenge the simplifications made in many subglacial hydrology models that treat moulin input as a point source at the ice-bed interface (e.g., Werder and others, 2013; de Fleurian and others, 2018; Sommers and others, 2018), and underscore the need for models to include englacial transport processes, potentially using constraints on typical englacial pathway lengths such as those revealed by our observations. Given that englacial storage can exert an important control on pressure dynamics within the subglacial drainage system (Flowers and Clarke, 2002a), accounting for these processes is crucial for accurate simulations of meltwater-driven glacier behavior.

Our study further demonstrates the value of high-density 3D GPR surveys for mapping both englacial and subglacial drainage structures. The ability to visualize and analyze the internal hydrological architecture in three dimensions provides critical insights that are not accessible through traditional 2D transects or indirect methods alone. Despite their clear potential, such 3D datasets remain rare in glaciological research, primarily because data acquisition has been time-consuming and logistically challenging (e.g., Church and others, 2020; Egli and others, 2021). However, with UAV-based radar systems, like the one used in this study, the collection of dense 3D datasets is now feasible. As survey technologies continue to evolve, there is a corresponding need for advancements in data processing workflows. In this study, we implement a novel diffraction imaging approach, drawing on state-of-the-art research in exploration seismology. The combination of high-frequency, high-resolution radar data with such advanced processing enables the detailed delineation of englacial structures. At present, robust 3D velocity estimation methods for common-offset GPR data remain limited, but their development represents a promising avenue for improving imaging accuracy in future studies (e.g., Bauer and others, 2017; Delf and others, 2022).

The above-described technological advancements open the door for repeat surveys, which have the potential to reveal temporal changes in both the englacial and subglacial drainage systems. Subglacially, such surveys could capture seasonal transitions from distributed to channelized flow, and assess the persistence or migration of subglacial channels over multiple seasons. Englacially, they could contribute to answering questions such as: Do englacial channels remain open throughout the year, close completely during winter or re-form each melt season in new locations? Are observed pathways persistent, or do they migrate or shift in response to hydrological or mechanical forcing over the course of the summer? Addressing these questions through repeat

https://doi.org/10.1017/jog.2026.10145 Published online by Cambridge University Press

3D imaging would provide a much-needed observational foundation for understanding the dynamics of internal water routing and the interplay between surface inputs, englacial transport and basal flow. Ultimately, such efforts are crucial for anticipating how glacier systems respond to climatic forcing through meltwater-driven feedbacks that influence ice flow, water storage and downstream discharge.

Conclusions

This study identified two primary subglacial drainage pathways (channels A and B) in the near-terminus zone of the Otemma Glacier. The positions of these basal conduits, derived from GPR bed reflection analysis, align well with flow paths estimated from hydraulic potential modeling. Dye tracing results confirmed rapid throughflow for most moulins, particularly those linked to channel A. In contrast, higher dispersion and slower velocities in channel B suggest a less efficient or more heterogeneous subglacial pathway.

Our observations show that englacial meltwater routing is structurally complex, involving lateral conduits, branching networks and localized pooling zones. We can infer that surface meltwater often travels substantial horizontal distances within the glacier before reaching the bed, supporting previous work that challenges the assumption of predominantly vertical flow. The presence of pooling zones highlights the role of englacial storage in modulating the timing and variability of meltwater delivery to the subglacial system. These dynamics should be explicitly accounted for when developing or refining models of subglacial hydrology and glacier dynamics, and when interpreting dye tracing results.

The unprecedented resolution, density and spatial extent of the acquired 3D GPR dataset in this study enabled direct imaging of both englacial and subglacial hydrological structures at high spatial resolution. New advanced processing strategies, adapted from reflection seismology, can bring immense value to glacier GPR imaging. In particular, diffraction imaging allowed us to resolve fine-scale features that would be challenging to identify with traditional GPR approaches. UAV-based GPR systems now enable efficient collection of dense 3D data, reducing logistical barriers and unlocking new opportunities for repeated surveys and larger-scale mapping of glacier hydrology. Repeat 3D surveys over the same region (i.e., 4D acquisitions) offer the potential to monitor the seasonal evolution of both the englacial and subglacial drainage systems, assess the persistence or reconfiguration of channels, and provide critical constraints on the temporal evolution of internal water routing.

Collectively, these findings support and extend theoretical models of glacier hydrology by providing observational evidence for englacial and subglacial routing and storage. Incorporating such processes into numerical models is essential for accurately simulating meltwater-driven feedbacks on ice flow and discharge, especially in the context of a changing climate, where this becomes increasingly important.

Data availability. The data that support the findings of this study are available from the corresponding author upon request.

Acknowledgements. We gratefully acknowledge Benjamin Schwarz and Alexander Bauer for providing diffraction imaging code and for their valuable assistance. We also thank Alana Bucheli and Luca Schärz for their support with photogrammetry processing. We appreciate the help with fieldwork from Mélissa Francey, Edith Sotelo Gamboa, Margaux Hofmann, Frédéric Lardet, Floreana Miesen and Pau Wiersma. This work was supported by the Swiss National Science Foundation (grant no. 188575) awarded to J. Irving.

References

Alley RB, Dupont TK, Parizek BR and Anandakrishnan S (2005) Access of surface meltwater to beds of sub-freezing glaciers: preliminary insights. *Annals of Glaciology* **40**(1), 8–14. doi: 10.3189/172756405781813483.

Allroggen N, Tronicke J, Delock M and Böniger U (2015) Topographic migration of 2D and 3D ground-penetrating radar data considering variable velocities. *Near Surface Geophysics* **13**(3), 253–259. doi: 10.3997/1873-0604.2014037.

Arcone SA and Yankielun NE (2000) 1.4 GHz radar penetration and evidence of drainage structures in temperate ice: Black Rapids Glacier, Alaska, U.S.A. *Journal of Glaciology* **46**(154), 477–490. doi: 10.3189/172756500781833133.

Bælum K and Benn DI (2011) Thermal structure and drainage system of a small valley glacier (Tellbreen, Svalbard), investigated by ground penetrating radar. *The Cryosphere* **5**(1), 139–149. doi: 10.5194/tc-5-139-2011.

Bartholomaus TC, Anderson RS and Anderson SP (2008) Response of glacier basal motion to transient water storage. *Nature Geoscience* **1**(1), 33–37.

Bartholomaus TC, Anderson RS and Anderson SP (2011) Growth and collapse of the distributed subglacial hydrologic system of Kennicott Glacier, Alaska, USA, and its effects on basal motion. *Journal of Glaciology* **57**(206), 985–1002.

Bartholomew I, Nienow P, Mair D, Hubbard A, King MA and Sole A (2010) Seasonal evolution of subglacial drainage and acceleration in a Greenland outlet glacier. *Nature Geoscience* **3**(6), 408–411.

Bauer A, Schwarz B and Gajewski D (2017) Utilizing diffractions in wavefront tomography. *Geophysics* **82**(2), R65-R73. doi: 10.1190/geo2016-0396.1.

Benn D, Gulley J, Luckman A, Adamek A and Glowacki PS (2009) Englacial drainage systems formed by hydrologically driven crevasse propagation. *Journal of Glaciology* **55**(191), 513–523. doi: 10.3189/002214309788816669.

Boon S and Sharp M (2003) The role of hydrologically-driven ice fracture in drainage system evolution on an Arctic glacier. *Geophysical Research Letters* **30**(18), 1916. doi: 10.1029/2003gl018034.

Boulton G, Morris E, Armstrong A and Thomas A (1979) Direct measurement of stress at the base of a glacier. *Journal of Glaciology* **22**(86), 3–24.

Bradford JH, Nichols J, Mikesell TD and Harper JT (2009) Continuous profiles of electromagnetic wave velocity and water content in glaciers: an example from Bench Glacier, Alaska, USA. *Annals of Glaciology* **50**(51), 1–9.

Burkimsher M (1983) Investigations of glacier hydrological systems using dye tracer techniques: Observations at Pasterzengletscher, Austria. *Journal of Glaciology* **29**(103), 403–416.

Catania GA, Neumann TA and Price SF (2008) Characterizing englacial drainage in the ablation zone of the Greenland ice sheet. *Journal of Glaciology* **54**(187), 567–578. doi: 10.3189/002214308786570854.

Chopra S and Marfurt KJ (2007) *Seismic Attributes for Prospect Identification and Reservoir characterization*. Society of Exploration Geophysicists and European Association of Geoscientists and Engineers. doi: 10.1190/1.9781560801900.

Church G, Bauder A, Grab M and Maurer H (2021) Ground-penetrating radar imaging reveals glacier's drainage network in 3D. *The Cryosphere* **15**(8), 3975–3988. doi: 10.5194/tc-15-3975-2021.

Church G, Grab M, Schmelzbach C, Bauder A and Maurer H (2020) Monitoring the seasonal changes of an englacial conduit network using repeated ground-penetrating radar measurements. *The Cryosphere* **14**(10), 3269–3286. doi: 10.5194/tc-14-3269-2020.

Clague JJ and O'Connor JE (2021) Chapter 14 - Glacier-related outburst floods. *In:* Haeberli W and Whiteman C (eds.), *Snow and Ice-Related Hazards, Risks, and Disasters*, 2nd Edn. Hazards and Disasters Series. Elsevier, 467–499.

de Fleurian B and 11 others (2018) SHMIP The subglacial hydrology model intercomparison project. *Journal of Glaciology* **64**(248), 897–916.

Delf R and 6 others (2022) Reanalysis of polythermal glacier thermal structure using radar diffraction focusing. *Journal of Geophysical Research: Earth Surface* **127**(2), e2021JF006382. doi: 10.1029/2021JF006382.

Egli PE, Irving J and Lane SN (2021) Characterization of subglacial marginal channels using 3-D analysis of high-density ground-penetrating radar data. *Journal of Glaciology* **67**(264), 759–772. doi: 10.1017/jog.2021.26.

Fischer M, Huss M and Hoelzle M (2015) Surface elevation and mass changes of all Swiss glaciers 1980–2010. *The Cryosphere* **9**(2), 525–540. doi: 10.5194/tc-9-525-2015.

Flowers GE and Clarke GKC (2002a) A multicomponent coupled model of glacier hydrology 1. Theory and synthetic examples. *Journal of Geophysical Research: Solid Earth* **107**(B11), 2287.

Flowers GE and Clarke GKC (2002b) A multicomponent coupled model of glacier hydrology 2. Application to Trapridge Glacier, Yukon, Canada. *Journal of Geophysical Research: Solid Earth* **107**(B11), 2288.

Flowers GE (2015) Modelling water flow under glaciers and ice sheets. *Proceedings of the Royal Society A: Mathematical, Physical and Engineering Sciences* **471**(2176), 20140907.

Fountain AG, Jacobel RW, Schlichting R and Jansson P (2005) Fractures as the main pathways of water flow in temperate glaciers. *Nature* **433**(7026), 618–621. doi: 10.1038/nature03296.

Fountain AG and Walder JS (1998) Water flow through temperate glaciers. *Reviews of Geophysics* **36**(3), 299–328. doi: 10.1029/97rg03579.

Gimbert F, Tsai VC, Amundson JM, Bartholomaus TC and Walter JI (2016) Subseasonal changes observed in subglacial channel pressure, size, and sediment transport. *Geophysical Research Letters* **43**(8), 3786–3794. doi: 10.1002/2016gl068337.

GLAMOS (1881-2023) *The Swiss Glaciers 1880-2022/23. Yearbooks of the Swiss Commission for Cryosphere observation (SKK) of the Swiss Academy of Sciences (SCNAT)*. Glaciological Reports No 1-142. Published since 1964 by VAW / ETH Zurich. doi: 10.18752/glrep_series.

GLIMS Consortium (2005) GLIMS Glacier Database, Version 1. National Snow and Ice Data Center. doi: 10.7265/N5V98602.

Grab M and 15 others (2021) Ice thickness distribution of all Swiss glaciers based on extended ground-penetrating radar data and glaciological modeling. *Journal of Glaciology* **67**(266), 1074–1092.

Gulley J and Benn DI (2007) Structural control of englacial drainage systems in Himalayan debris-covered glaciers. *Journal of Glaciology* **53**(182), 399–412. doi: 10.3189/002214307783258378.

Gulley J (2009) Structural control of englacial conduits in the temperate Matanuska Glacier, Alaska, USA. *Journal of Glaciology* **55**(192), 681–690. doi: 10.3189/002214309789470860.

Gulley JD, Benn DI, Müller D and Luckman A (2009a) A cut-and-closure origin for englacial conduits in uncrevassed regions of polythermal glaciers. *Journal of Glaciology* **55**(189), 66–80. doi: 10.3189/002214309788608930.

Gulley JD, Benn DI, Screaton E and Martin J (2009b) Mechanisms of englacial conduit formation and their implications for subglacial recharge. *Quaternary Science Reviews* **28**(19), 1984–1999. doi: 10.1016/j.quascirev.2009.04.002.

Hagen JO, Liestøl O, Sollid JL, Wold B and Østrem G (1993) Subglacial investigations at Bondhusbreen, Folgefonni, Norway. *Norwegian Journal of Geography* **47**(3), 117-162.

Hansen LU, Piotrowski JA, Benn DI and Sevestre H (2020) A cross-validated three-dimensional model of an englacial and subglacial drainage system in a High-Arctic glacier. *Journal of Glaciology* **66**(256), 278–290. doi: 10.1017/jog.2020.1.

Harper JT, Bradford JH, Humphrey NF and Meierbachtol TW (2010) Vertical extension of the subglacial drainage system into basal crevasses. *Nature* **467**(7315), 579–582. doi: 10.1038/nature09398.

Hart JK, Rose KC, Clayton A and Martinez K (2015) Englacial and subglacial water flow at Skálafellsjökull, Iceland derived from ground penetrating radar, in situ Glacsweb probe and borehole water level measurements. *Earth Surface Processes and Landforms* **40**(15), 2071–2083. doi: 10.1002/esp.3783.

Hewitt I (2013) Seasonal changes in ice sheet motion due to melt water lubrication. *Earth and Planetary Science Letters* **371** 16–25.

Hock R, Iken L and Wangler A (1999) Tracer experiments and borehole observations in the over-deepening of Aletschgletscher, Switzerland. *Annals of Glaciology* **28**(1), 253–260. doi: 10.3189/172756499781821742.

Hodge SM (1976) Direct measurement of basal water pressures: a pilot study. *Journal of Glaciology* **16**(74), 205–218. doi: 10.3189/S0022143000031543.

Holmlund P (1988) Internal geometry and evolution of moulins, Storglaciären, Sweden. *Journal of Glaciology* **34**(117), 242–248. doi: 10.3189/S0022143000032305.

Hubbard B, Sharp M, Willis I, Nielsen M and Smart C (1995) Borehole water-level variations and the structure of the subglacial hydrological system of Haut Glacier d'Arolla, Valais, Switzerland. *Journal of Glaciology* **41**(139), 572–583.

Iken A (1972) Measurements of water pressure in moulins as part of a movement study of the White Glacier, Axel Heiberg Island, Northwest Territories, Canada. *Journal of Glaciology* **11**(61), 53–58. doi: 10.3189/S0022143000022486.

Iken A and Truffer M (1997) The relationship between subglacial water pressure and velocity of Findelengletscher, Switzerland, during its advance and retreat. *Journal of Glaciology* **43**(144), 328–338.

Irvine-Fynn TDL, Moorman BJ, Williams JLM and Walter FSA (2006) Seasonal changes in ground-penetrating radar signature observed at a polythermal glacier, Bylot Island, Canada. *Earth Surface Processes and Landforms* **31**(7), 892–909. doi: 10.1002/esp.1299.

Jenkin M and 6 others (2023) Tracking coarse sediment in an alpine subglacial channel using radio-tagged particles. *Journal of Glaciology* **69**(278), 1992–2006. doi: 10.1017/jog.2023.77.

Langhammer L, Rabenstein L, Bauder A and Maurer H (2017) Ground-penetrating radar antenna orientation effects on temperate mountain glaciers. *Geophysics* **82**(3), H15-H24.

Lappegard G, Kohler J, Jackson M and Hagen JO (2006) Characteristics of subglacial drainage systems deduced from load-cell measurements. *Journal of Glaciology* **52**(176), 137–148. doi: 10.3189/172756506781828908.

Lefeuvre PM, Jackson M, Lappegard G and Hagen JO (2015) Interannual variability of glacier basal pressure from a 20 year record. *Annals of Glaciology* **56**(70), 33–44.

Lindner F, Walter F, Laske G and Gimbert F (2020) Glaciohydraulic seismic tremors on an Alpine glacier. *The Cryosphere* **14**(1), 287–308. doi: 10.5194/tc-14-287-2020.

Mankoff KD and 7 others (2017) Roughness of a subglacial conduit under Hansbreen, Svalbard. *Journal of Glaciology* **63**(239), 423–435. doi: 10.1017/jog.2016.134.

Moorman BJ and Michel FA (2000) Glacial hydrological system characterization using ground-penetrating radar. *Hydrological Processes* **14**(15), 2645–2667.

Murray T, Stuart GW, Fry M, Gamble NH and Crabtree MD (2000) Englacial water distribution in a temperate glacier from surface and borehole radar velocity analysis. *Journal of Glaciology* **46**(154), 389–398. doi: 10.3189/172756500781833188.

Nanni U and 6 others (2020) Quantification of seasonal and diurnal dynamics of subglacial channels using seismic observations on an Alpine glacier. *The Cryosphere* **14**(5), 1475–1496. doi: 10.5194/tc-14-1475-2020.

Nienow P, Sharp M and Willis I (1996a) Sampling-rate effects on the properties of dye breakthrough curves from glaciers. *Journal of glaciology* **42**(140), 184–189.

Nienow P, Sharp M and Willis I (1996b) Temporal switching between englacial and subglacial drainage pathways: Dye tracer evidence from the Haut Glacier d'Arolla, Switzerland. *Geografiska Annaler: Series A, Physical Geography* **78**(1), 51–60.

Nienow P, Sharp M and Willis I (1996c) Velocity–discharge relationships derived from dye tracer experiments in glacial meltwaters: Implications for subglacial flow conditions. *Hydrological Processes* **10**(10), 1411–1426.

Nienow P, Sharp M and Willis I (1998) Seasonal changes in the morphology of the subglacial drainage system, Haut Glacier d'Arolla, Switzerland. *Earth Surface Processes and Landforms* **23**(9), 825–843.

O'Callaghan JF and Mark DM (1984) The extraction of drainage networks from digital elevation data. *Computer vision, graphics, and Image processing* **28**(3), 323–344.

Ogier C and 6 others (2023) Ground penetrating radar in temperate ice: englacial water inclusions as limiting factor for data interpretation. *Journal of Glaciology* **69**(278), 1874–1885.

Plewes LA and Hubbard B (2001) A review of the use of radio-echo sounding in glaciology. *Progress in Physical Geography Earth and Environment* **25**(2), 203–236.

Rada Giacaman CA and Schoof C (2023) Channelized, distributed, and disconnected: spatial structure and temporal evolution of the subglacial drainage under a valley glacier in the Yukon. *The Cryosphere* **17**(2), 761–787.

Ruols B, Baron L and Irving J (2023) Development of a drone-based ground-penetrating radar system for efficient and safe 3D and 4D surveying of alpine glaciers. *Journal of Glaciology* **69**, 1–12. doi: 10.1017/jog.2023.83.

Ruols B, Klahold J, Farinotti D and Irving J (2025) 4D GPR imaging of a near-terminus glacier collapse feature. *The Cryosphere* **19**(9), 4045–4059. doi: 10.5194/tc-19-4045-2025.

Schaap T, Roach MJ, Peters LE, Cook S, Kulessa B and Schoof C (2020) Englacial drainage structures in an East Antarctic outlet glacier. *Journal of Glaciology* **66**(255), 166–174. doi: 10.1017/jog.2019.92.

Schneider WA (1978) Integral formulation for migration in two and three dimensions. *Geophysics* **43**(1), 49–76.

Schoof C (2010) Ice-sheet acceleration driven by melt supply variability. *Nature* **468**(7325), 803–806.

Schroeder DM and 9 others (2020) Five decades of radioglaciology. *Annals of Glaciology* **61**(81), 1–13.

Schwanghart W and Kuhn NJ (2010) Topotoolbox: A set of Matlab functions for topographic analysis. *Environmental Modelling & Software* **25**(6), 770–781.

Schwanghart W and Scherler D (2014) TopoToolbox 2–MATLAB-based software for topographic analysis and modeling in Earth surface sciences. *Earth Surface Dynamics* **2**(1), 1–7.

Schwarz B and Gajewski D (2017) Accessing the diffracted wavefield by coherent subtraction. *Geophysical Journal International* **211**(1), 45–49. doi: 10.1093/gji/ggx291.

Schwarz B (2019) Coherent wavefield subtraction for diffraction separation. *Geophysics* **84**(3), doi: 10.1190/geo2018-0368.1.

Selbesoğlu MO and 11 others (2023) Accuracy assessment of glacier depth monitoring based on UAV-GPR on Horseshoe Island, Antarctica. *Turkish Journal of Earth Sciences* **32**(8), 999–1012.

Shreve R (1972) Movement of water in glaciers. *Journal of Glaciology* **11**(62), 205–214.

Sommers A, Rajaram H and Morlighem M (2018) SHAKTI: subglacial hydrology and kinetic, transient interactions v1. 0. *Geoscientific Model Development* **11**(7), 2955–2974.

Stenborg T (1969) Studies of the internal drainage of glaciers. *Geografiska Annaler: Series A, Physical Geography* **51**(1-2), 13–41. doi: 10.1080/04353676.1969.11879788.

Stenborg T (1973) Some viewpoints on the internal drainage of glaciers. *Hydrology of Glacier* **95**, 117–129.

Stuart G, Murray T, Gamble N, Hayes K and Hodson A (2003) Characterization of englacial channels by ground-penetrating radar: An example from austre Brøggerbreen, Svalbard. *Journal of Geophysical Research: Solid Earth* **108**(B11), 2525. doi: 10.1029/2003jb002435.

Taner MT, Koehler F and Sheriff R (1979) Complex seismic trace analysis. *Geophysics* **44**(6), 1041–1063.

Temminghoff M, Benn DI, Gulley JD and Sevestre H (2019) Characterization of the englacial and subglacial drainage system in a high Arctic cold glacier by speleological mapping and ground-penetrating radar. *Geografiska Annaler: Series A, Physical Geography* **101**(2), 98–117. doi: 10.1080/04353676.2018.1545120.

Tjoelker AR and 6 others (2024) Drone-based ground-penetrating radar with manual transects for improved field surveys of buried ice. *Remote Sensing* **16**(13), 2461.

Valence E, Baraer M, Rosa E, Barbecot F and Monty C (2022) Drone-based ground-penetrating radar (GPR) application to snow hydrology. *The Cryosphere* **16**(9), 3843–3860.

van der Veen CJ (2007) Fracture propagation as means of rapidly transferring surface meltwater to the base of glaciers. *Geophysical Research Letters* **34**(1), L01501. doi: 10.1029/2006gl028385.

Vivian R and Bocquet G (1973) Subglacial cavitation phenomena under the Glacier d'Argentière, Mont Blanc, France. *Journal of Glaciology* **12**(66), 439–451.

Walder J and Hallet B (1979) Geometry of former subglacial water channels and cavities. *Journal of Glaciology* **23**(89), 335–346. doi: 10.3189/S0022143000029944.

Werder MA, Hewitt IJ, Schoof CG and Flowers GE (2013) Modeling channelized and distributed subglacial drainage in two dimensions. *Journal of Geophysical Research: Earth Surface* **118**(4), 2140–2158.

Woodward J and Burke MJ (2007) Applications of ground-penetrating radar to glacial and frozen materials. *Journal of Environmental & Engineering Geophysics* **12**(1), 69–85.

https://doi.org/10.1017/jog.2026.10145 Published online by Cambridge University Press